

# Growth and Etching of Monolayer Hexagonal Boron Nitride

Lifeng Wang, Bin Wu, Lili Jiang, Jisi Chen, Yongtao Li, Wei Guo, Pingan Hu,\* and Yunqi Liu\*

2D materials have attracted significant attention due to their super properties and great potentials for various applications.<sup>[1,2]</sup> It is critical to achieve precise synthesis controls over these materials' parameters and related physical properties. Especially, chemical vapor deposition (CVD) method has emerged as a versatile platform for growing various 2D materials. The method generally results in a growth of 2D materials on a supporting substrate, which potentially modifies the intrinsic properties of as-grown materials depending largely on the interaction between two adjacent materials. On the other hand, this method provides a plenty space of adjustability for the final product and allows as-grown 2D materials on substrate to be further processed for certain purpose. As an example, various parameters of graphene such as crystallinity, size, edge structure, shape/morphology, and layer number were found to be manipulated to some degree by tuning the growth process or introducing the external modifications of substrates, precursors, and others.<sup>[3,4]</sup> However, understanding the underlying mechanism and connection behind various, apparently different phenomena remains challenging as the growth process involves multiple complex microscopic processes.

In general, CVD growth of 2D materials on heterogeneous surface falls into three modes established in thin film growth from the thermodynamic point of view, and these modes include island formation, layer-by-layer, and layer-plus-island depending on the interaction between surface and adatoms. In particular, graphene grown on Cu by CVD method is similar to the case of layer-by-layer mode due to the extreme low solubility of carbon in bulk Cu.<sup>[5,6]</sup> The recognition of this surface nucleation and growth mechanism has important applications in partly understanding the correlation among experimental conditions and the resulting growth behaviors and designing the proper strategies for precise controls over the resulting

product. For example, nucleation density of graphene can be controlled by engineering substrate surface properties or CVD growth process parameters as nucleation preferentially occurs on locations with high surface energy such as defect or grain boundaries.<sup>[7,8]</sup> However, the description of this growth mechanism is essentially based on a thermodynamic point, which is not capable to explain and predict rich, complex observations of 2D materials' morphologies in a wide growth window or the coalescence process of separated flakes. For an entire picture, a bird's eye view of kinetic growth process is essential though much less attention has been drawn on this aspect in previous work.

Along this line, our previous studies on graphene growth and etching on liquid Cu have indicated that graphene growth stage is governed by the competition between attachment kinetics and adatom diffusion-controlled process.<sup>[9,10]</sup> The modulation of these processes leads to well-defined evolution of graphene shape or etched patterns characterized ranging from Euclidian to fractal geometry. In this sense, 2D material growth systems provide ideal and true cases that only exist in imagined textbook model for crystal growth study, and it would be fundamentally important to know whether this principle is general regardless of the grown 2D material composition. Being an important 2D insulator with a large bandgap ( $\approx 6$  eV),<sup>[11]</sup> monolayer h-BN has many distinct physical properties, making it a super dielectric for enhancing graphene electronic device quality. Relevantly and importantly, h-BN has similar lattice structure (a lattice mismatch of only 1.6% known as "white graphene") with graphene, but with reduced threefold symmetry due to the existence of two kinds of atoms B and N. The similarity and difference of h-BN with respect to graphene justify the importance in exploring its fundamental growth mechanism in addition to its usefulness. Recently, h-BN films have been grown on metal substrate (Cu, Ni, Pt.) by CVD method.<sup>[12–23]</sup> In analogy to graphene growth, various shaped h-BN domains were observed including triangular,<sup>[12,18–23]</sup> asymmetric diamond<sup>[17]</sup> or hexagonal<sup>[23]</sup> shapes by changing the growth parameters, such as temperature of the precursor, growth time, and pressure of CVD system.

Here, we report the intrinsic behaviors of CVD grown monolayer h-BN shape evolution and etched h-BN patterns using a CVD grown monolayer h-BN on Cu foil. The shapes of h-BN domains can be modulated from triangle with straight edges to negative curved and to positive curved edges by adjusting the heating temperature of the source ( $\text{BH}_3\text{-NH}_3$ ). The etched patterns of monolayer h-BN follows anisotropic rules under pure  $\text{H}_2$  condition, while changing  $\text{Ar}/\text{H}_2$  flow rate ratio leads to complex fractal etching behavior for monolayer h-BN. These results demonstrate that the growth and etching kinetics of h-BN share the common physics with the graphene case at a fundamental level. Moreover, this principle is successfully applied to explain the dynamic formation of complex

L. Wang, Prof. P. Hu  
School of Materials Science and Engineering  
Harbin Institute of Technology  
Harbin 150080, P. R. China  
E-mail: hupa@hit.edu.cn

L. Wang, Prof. P. Hu  
Key Lab of Microsystem and Microstructure  
Ministry of Education  
Harbin Institute of Technology  
Harbin 150080, P. R. China

L. Wang, Dr. B. Wu, L. Jiang, J. Chen, Y. Li, W. Guo, Prof. Y. Liu  
Beijing National Laboratory for Molecular Sciences  
Key Laboratory of Organic Solids  
Institute of Chemistry  
Chinese Academy of Science  
Beijing 100190, P. R. China  
E-mail: liuyq@iccas.ac.cn



DOI: 10.1002/adma.201501166

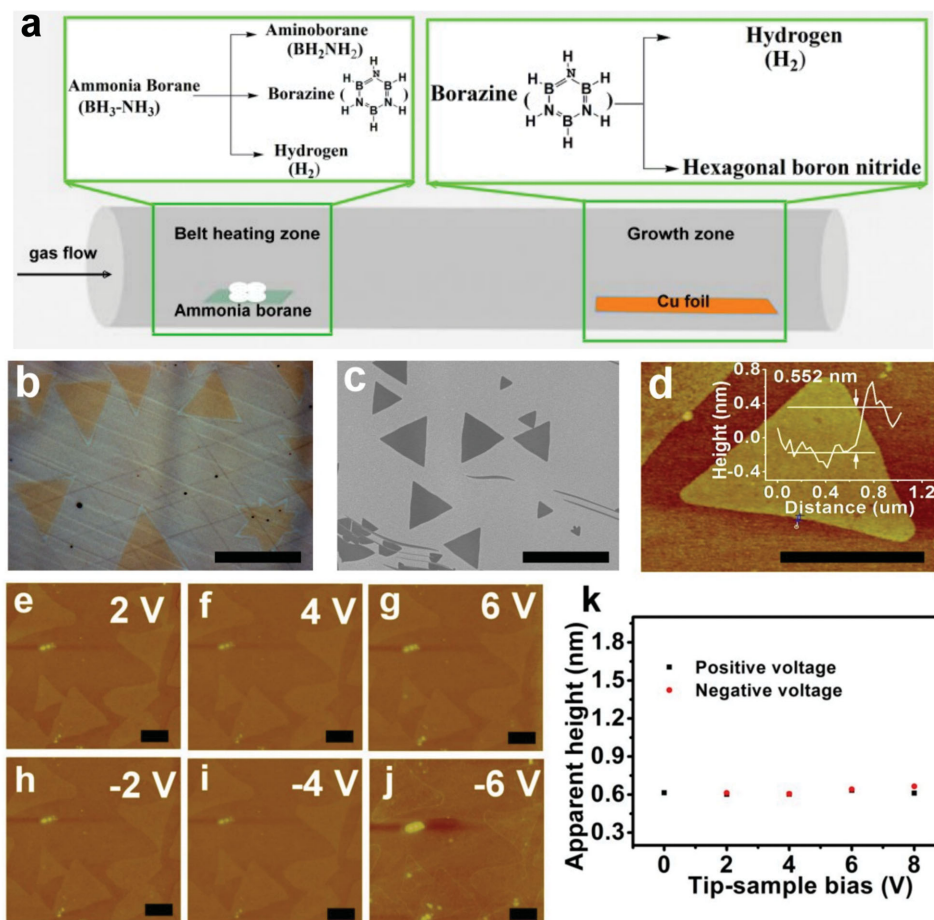


**Figure 1.** a) Schematic showing the CVD setup. b,c) the optical and SEM images of triangle-shaped h-BN flakes on Cu surface, respectively. Note that h-BN/Cu in (b) was air-oxidized for increasing the optical contrast. The scale bars are 10  $\mu\text{m}$ . d) AFM image of h-BN flakes transferred onto  $\text{SiO}_2/\text{Si}$  substrate, followed by 0.5 h air oxidation at 950  $^\circ\text{C}$  for the removal of surface impurities. The scale bar is 10  $\mu\text{m}$ . e–j) A series of tapping mode AFM height images of monolayer h-BN flakes using different biased tip. k) The apparent height of h-BN as a function of tip bias. The scale bars are 1  $\mu\text{m}$ .

structures composed of the merged triangles via the coalescence process among separated h-BN domains.

Our CVD approach for the growth of monolayer h-BN involves a low pressure condition, the use of solid ammonia borane as precursors and solid Cu substrate as schematically shown in Figure 1a. Briefly, precursor molecules are heated to dissociate into hydrogen, polyiminoborane ( $\text{BH}_2\text{NH}_2$ ; solid), and borazine ( $(\text{HBNH})_3$ ; gas),<sup>[12–20,24,25]</sup> which involves the formation of h-BN on Cu surface in reaction chamber. Similar to our previously reported results,<sup>[12]</sup> triangle-shaped h-BN with straight edges can be formed on Cu surface under pure Ar carrier gas with a flow of about 40 sccm (standard cubic centimeter per minute) at the growth temperature of 1000  $^\circ\text{C}$  and a pressure of about 30–40 Pa. Figure 1b,c shows the optical and scanning electron microscopic (SEM) images of as-grown h-BN domains on Cu surface, respectively. Figure 1d shows a typical atomic force microscopic (AFM) image of triangle h-BN transferred onto 300 nm  $\text{SiO}_2/\text{Si}$  substrate. The typical thickness of h-BN is measured to be about 0.55 nm, confirming its monolayer property. Monolayer and single crystal characteristic within a region of h-BN film were further confirmed by the same set of sixfold diffraction patterns recorded at three

random selected points (Figure S1, Supporting Information) on film. Atomic scale imaging of h-BN grown on Cu was also explored using scanning tunneling microscopy (STM) technique. An almost defect-free area is provided in Figure S2, Supporting Information, showing the characteristic h-BN lattice constant of 0.253 nm. Figure S3, Supporting Information, shows X-ray photoemission spectroscopy (XPS) measurements of h-BN film on Cu. The binding energies of 397.96 and 190.26 eV can be attributed to N 1s and B 1s, respectively, which are in good agreement with the literature values.<sup>[16–20]</sup> The B/N ratio from our XPS survey was estimated to be 1.07.

The quality of h-BN film can be evaluated by testing its resistance. It has previously been reported that carbon impurities can depress the insulating nature of h-BN and allow current flow through the carbon-doped layers.<sup>[26,27]</sup> Different from traditional direct current–voltage ( $I$ – $V$ ) measurement, we qualitatively evaluated sample's conductivity by an indirect and fast method based on biased tip tapping mode AFM imaging.<sup>[28]</sup> Figure 1e–k shows a series of height images of transferred h-BN flakes on 300 nm  $\text{SiO}_2/\text{Si}$  substrate taken with AFM tip biased from positive (2 to 6 V) to negative voltage (–2 to –6 V). The apparent heights under all negative or positive

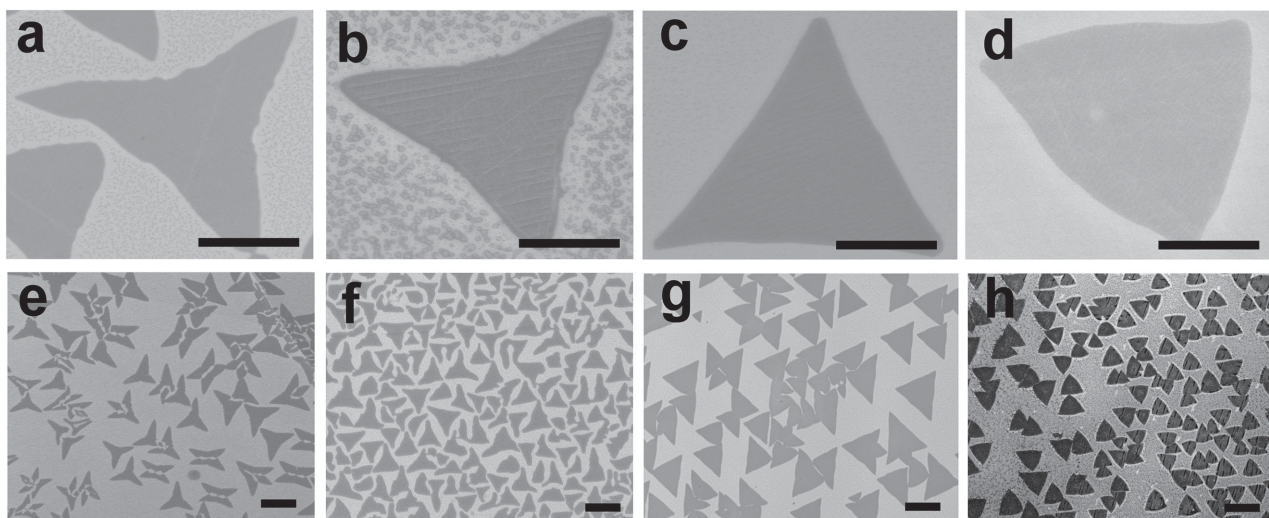


**Figure 2.** a–d) SEM images of various-shaped h-BN domains grown on annealed Cu foil surface under different belt heating temperature of 50, 70, 90, and 110 °C, respectively. The scale bars are 5 μm. e–h) The corresponding large scale SEM images of well-dispersed h-BN flakes with different morphologies. The scale bars are 10 μm.

biased tip were almost same to that (0.62 nm, Figure S4, Supporting Information) under the unbiased tip. The increase of apparent height of samples imaged by a biased tip can be used to qualitatively distinguish sample's conductivity, i.e., the lower increase the less conductivity of sample is. This result shows that h-BN sample is a better insulator than the reported insulating graphene oxide measured by this method, indicating that our h-BN sample is of high quality.

With triangular h-BN flake as a well-defined morphology reference, we explored the effect of different temperatures of heating belt (for example,  $T = 50, 70, 90$ , and  $110$  °C) on the shape evolution of the resulting sample while keeping other growth parameters unchanged. Figure 2a–d and e–h shows a series of typical individual and the corresponding large-scale SEM images of h-BN flakes grown on Cu surfaces as a function of the different heating belt temperatures (see the details in Table S1, Supporting Information), respectively. At the heating belt temperature of  $90$  °C, triangle-shaped h-BN flakes with straight edges were formed (Figure 2c), and the morphology of each h-BN domain is highly uniform and reproducible (Figure 2g). Using a higher temperature ( $T = 110$  °C) resulted in a triangle-shaped backbone with positive curved edges (Figure 2d). With decreasing the temperature ( $T = 70$  and  $50$  °C), the morphologies of h-BN flakes with respect to perfect triangle gradually change into those with more negative curved edges (Figure 2a,b). The intriguing feature in these results is that the whole set of h-BN morphologies are geometrically connected, following a clear shape evolution rule. Ideally, the invariant in the shape evolution is threefold symmetry which reflects the symmetry of h-BN microscopic lattice, and the variable is edge curvature in a first approximation. In this sense, the observed specific morphology of h-BN flakes is a specific example of a general unlimited set of morphologies, and in practice, it would be very useful to produce the desired shape under the guidance of this empirical rule.

This shape evolution trend is indeed in analogy to those for many other material growth systems such as thin film growth of

various materials, snow crystal, and graphene flake regardless of different growth processes involved in each cases. The entire set of compact triangle and fractal structures indicates that the growth dynamics evolves from attachment-kinetics dominated growth to diffusion-controlled mode that has been coined several decades before.<sup>[29]</sup> Based on this growth mechanism, a picture of kinetic growth of h-BN is proposed to take account of shape evolution as follows. As confirmed previously,<sup>[12]</sup> it is necessary for borazine precursors to dehydrogenate to form the h-BN lattice. In this case, certain concentration of the building blocks adsorbed on Cu surface would initiate the h-BN nucleation process, followed by growth stage that is controlled by various microscopic kinetic processes. In our case, the role of the heating belt is to directly modulate the concentrations of h-BN building blocks, thus affecting adatom surface diffusion kinetics. The low concentration favors diffusion-limited growth, leading to a branched or fractal (negative curved edges) structure instead of compact, regular triangle h-BN. On the other hand, too high concentration of adatoms results in the isotropic growth (Figure 2d) due to a uniform concentration distribution of adatoms along the circumference of h-BN nuclei. In addition, we found that the nucleation density of h-BN increased as a function of the temperature of the heating belt (Figure S5, Supporting Information), which is consistent with changes of h-BN precursor concentrations in this process. Figure S6, Supporting Information, shows the corresponding size distribution of h-BN domains in which a larger size is produced using the belt temperature of  $90$  °C.

For comparison, we further performed the detailed study on the reverse process of h-BN growth, i.e., etching. While etching itself is practically important for fabricating the patterned materials, in contrast to graphene etching study, h-BNs etching behavior is largely unknown at present.<sup>[30]</sup> To elucidate the etching behavior of monolayer h-BN, we investigated a series of systematic experiments involving the etching of continuous monolayer h-BN and individual triangle-shaped h-BN flakes by varying the ratio of Ar/H<sub>2</sub> gas (H<sub>2</sub> molecules are expected to

AFM偏置  
探针？样  
品导电  
性？



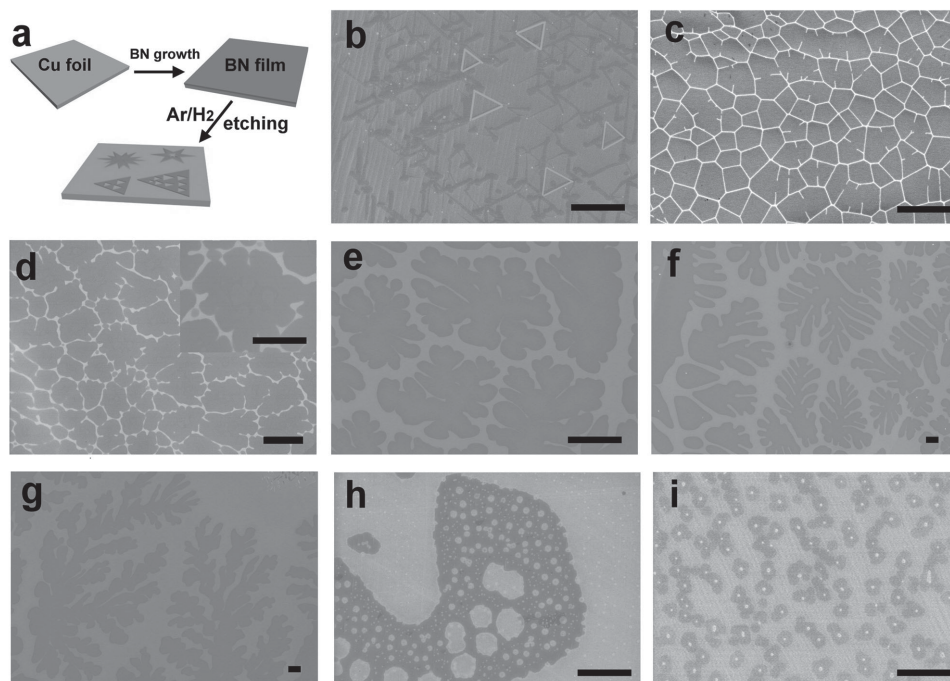


**Figure 3.** a) Schematic showing the process of h-BN growth on Cu surface and subsequent etching using different Ar/H<sub>2</sub> flow ratios. b–g) Typical SEM images of a series of etched h-BN patterns with different shapes using various increased Ar/H<sub>2</sub> flow rate ratios. h,i) Well- and poorly-defined etched holes on monolayer h-BN using pure H<sub>2</sub> and Ar gas at a low pressure of 30–40 Pa, respectively. All the scale bars are 10 μm.

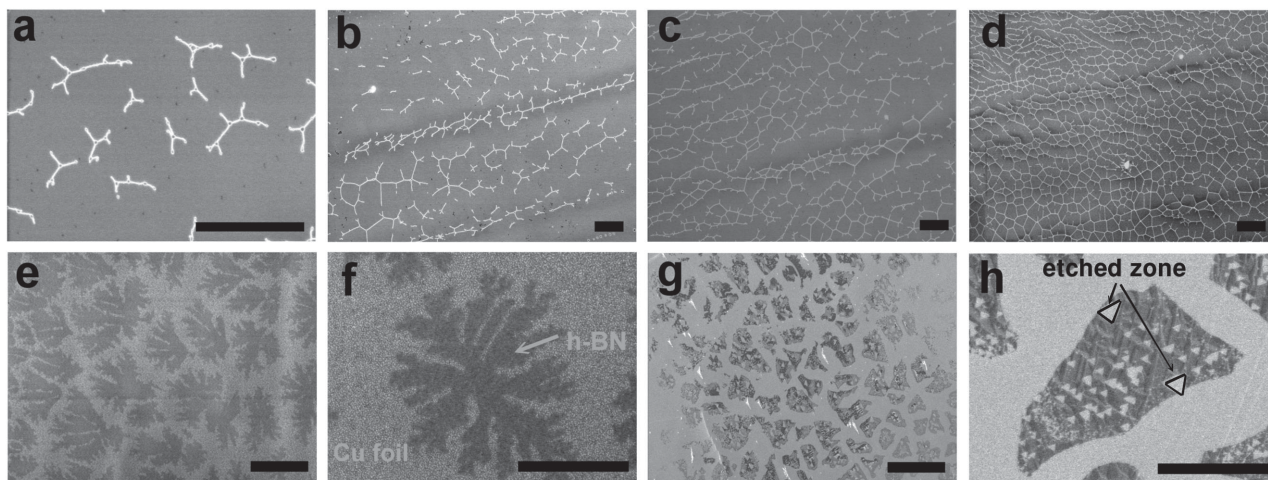
be etchant of h-BN) at 1000 °C at low and ambient pressure CVD conditions. As schematically shown in **Figure 3a**, when monolayer h-BN film or separated h-BN flakes were grown on Cu surface, the heating of precursors was turned off. Then different ratios of Ar/H<sub>2</sub> flow were introduced into the system for a period of time while keeping the temperature unchanged. Finally, the furnace was quickly cooled down to room temperature under H<sub>2</sub> gas condition.

Figure 3b–g shows a series of SEM images of typical etched patterns on continuous monolayer h-BN under different Ar/H<sub>2</sub> flow ratios at ambient pressure (see Table S2 in the Supporting Information). When pure H<sub>2</sub> (Ar/H<sub>2</sub> = 0/300 sccm) was applied in the etching stage (Figure 3b), most part of continuous h-BN film was etched away, leaving straight lines on Cu surface. These lines essentially form 60° angles between them, and within some regions, etched single triangle or jointed triangles can be easily identified (labeled in Figure 3b), demonstrating that h-BN etching in this case is anisotropic and only related to the lattice structure of h-BN. Increasing Ar/H<sub>2</sub> flow rate ratio resulted in a dramatic change of etched patterns. For example, using Ar/H<sub>2</sub> flow rate ratio (800/300) led to etched continuous network composed of lines (white lines in Figure 3c), in addition, some of branched short etched lines that were nucleated along the main network and pointed into other directions were also observed. With further increasing the Ar/H<sub>2</sub> flow rate ratio (Figure 3d–g and Figure S7, Supporting Information), non-etched h-BN films have more and more opened structure with flower-like morphology characterized by fractal geometry.

The h-BN etching at a low pressure of 30–40 Pa was also explored as shown in Figure 3h,i. First, quasi-hexagonal patterns were etched on monolayer h-BN at pure H<sub>2</sub> condition,

which is different from the case at the corresponding ambient pressure. Second, using pure Ar condition resulted in the poorly defined etched pattern, which is in sharp contrast to the etching case at ambient pressure.

It should be important to recognize that although detailed etched anisotropic and fractal patterns are quite different in graphene,<sup>[9]</sup> h-BN etching at low and ambient pressure cases, i.e., the observations that h-BN etching modes vary from anisotropic to fractal etching with increasing the amount of Ar gas indeed support the hypothesis that diffusion-controlled process is applied to h-BN etching cases. **Figure 4a–d** shows a typical example that monolayer h-BN was etched with time. The corresponding plot of the percent of etched part in the whole h-BN area with etching time is shown in Figure S8, Supporting Information. It can be clearly seen that simple etched, branched line structures were firstly formed, developed and eventually connected. In the case of etching on individual h-BN flakes, the final fractal structure for non-etched part is similar to those observed on h-BN film (Figure 3e,f). The etching of individual h-BN flakes at pure H<sub>2</sub> condition resulted in the small triangle holes (Figure 4g,h), which is also consistent with the case for h-BN film etching shown in Figure 4b. In addition, the etched triangular pits are oriented in the same direction with relatively uniform distribution. According to these results, we could conclude that the triangle-shaped h-BN flakes are single crystal, which is consistent with results of our TEM tests. Finally, increasing etching temperature from 1000 to 1050 °C resulted in a larger etched triangle holes as shown in Figure S9, Supporting Information. This simple etching method provides a way to estimate the crystallinity of single crystal h-BN flake, or construct aligned etched pattern within the h-BN films.

Ar:H<sub>2</sub>=800:300

**Figure 4.** a–d) Evolution of etched patterns on h-BN film under the condition of Figure 3c shown in Table S2, Supporting Information. e,f) Large scale and zoom-in SEM images of etched patterns on individual h-BN flakes under pure 200 sccm Ar gas flow. g,h) Large scale and zoom-in SEM images of etched patterns on individual h-BN flakes under 200 sccm H<sub>2</sub> gas flow at 1000 °C. All the scale bars are 10 μm.

The above analysis for explaining the formation mechanism of h-BN etched pattern is essentially independent of specific etchants for h-BN. Among many species existed in the system including H<sub>2</sub>, Ar, atomic H, residual O<sub>2</sub> or H<sub>2</sub>O species, the most likely etchant for h-BN is atomic hydrogen, which has been proposed and supported by previous experimental work.<sup>[31]</sup> In our case, Raman and Fourier transform infrared (FTIR) spectra were taken on h-BN samples before and after etching. Both samples show a characteristic peak around 1368 cm<sup>-1</sup> for h-BN (Figure S10, Supporting Information), demonstrating that the sp<sup>2</sup> bonded hexagonal lattice of BN remains after etching. FTIR spectra of both samples (Figure S11, Supporting Information) directly taken from h-BN film/Cu substrate are similar, showing two peaks at 1370 and 833 cm<sup>-1</sup> attributed to vibration modes for a sp<sup>2</sup>-bonded BN.<sup>[31,32]</sup> These results indicate that active etchant simply takes away B and N atoms without introducing the significant functionality or structure modification of h-BN samples.

In as-grown samples, in addition to high yield separated triangle h-BN flakes, many kinds of abnormal and complex structures were also observed (Figure 5). These observations are not unique in h-BN growth, and were also confirmed in the case of CVD grown WS<sub>2</sub><sup>[33]</sup> and MoS<sub>2</sub>.<sup>[34,35]</sup> However, the formation process remains unexplained, even at a qualitative level. Figure 5a–e shows the typical complex structures of h-BN flakes grown on Cu surface. These structures appear to be combinations of different triangles via coalescence process, representing a final merged state. In order to investigate their specific coalescence process, a large number of SEM images were carefully analyzed to find the different intermediate states in the coalescent process.

In principle, there are two kinds of merging possibilities for triangle-shaped h-BN flakes including point-to-edge and edge-to-edge modes. Figure 5f–j shows these merging cases that are indicated by arrows in each SEM image, and illustrate several interesting and important points. First, when two adjacent h-BN flakes are certain distance away, each growth appears to be independent with the other and no effect on the changes of

h-BN flake morphologies was observed. Second, when adjacent h-BN flakes are close enough, the edge of h-BN flakes within adjacent region becomes negatively curved. This observation has never been revealed before, but is very general with a solid confirmation by a large number of SEM image survey. In the case of point to edge merging mode, the edge curves toward negative direction, while other two edges of the same h-BN flake remain the original state (Figure 5f,g). In the case of edge-to-edge merging, both edges of h-BN flakes evolve into negative curved edges while others remain unchanged (Figure 5f–h). Finally, Figure 5i,j shows various cases of point-to-edge or edge-to-edge modes approaching the final merged states with very narrow gaps left. The planar geometry of each h-BN flakes is complementary to each other, forming lock and key structures.

The above results show the evidences for the states of merged h-BN flakes at different stages from well-separated, closely distanced to seamless connected states. From these observations, we can gain an insight into the underlying physics as follows. In general, when a small intrusion is developed on a straight faceted edge of the grown materials, adatom diffusion will supply material to the very tip of intrusion at a faster rate than to the surrounding flat edge, leading to negatively curved edge. This positive feedback effect is universal, and known as the Mullins–Sekerka instability.<sup>[29]</sup> In our merging cases of h-BN flakes, the intriguing feature is that the surrounding part of h-BN straight edge is occupied by adjacent h-BN flake surface. Our experimental observations strongly support the idea that the surface of adjacent h-BN flake blocks adatom surface diffusion compared to Cu surface, which is much like the case that a block changes the fluid path. Due to Mullins–Sekerka effect and modified local diffusion path of adatoms in h-BN growth system, adjacent parts of different h-BN flakes continuously adjust their curvatures as a function of separated distance and evolved local space shape caused by net material growth, leading to complementary lock and key structure that is eventually merged. Indeed, the curved edges of h-BN flakes reflect a profile of local concentration distribution of precursors. Based on this analysis, we can establish a model to describe the process of h-BN flake coalescence



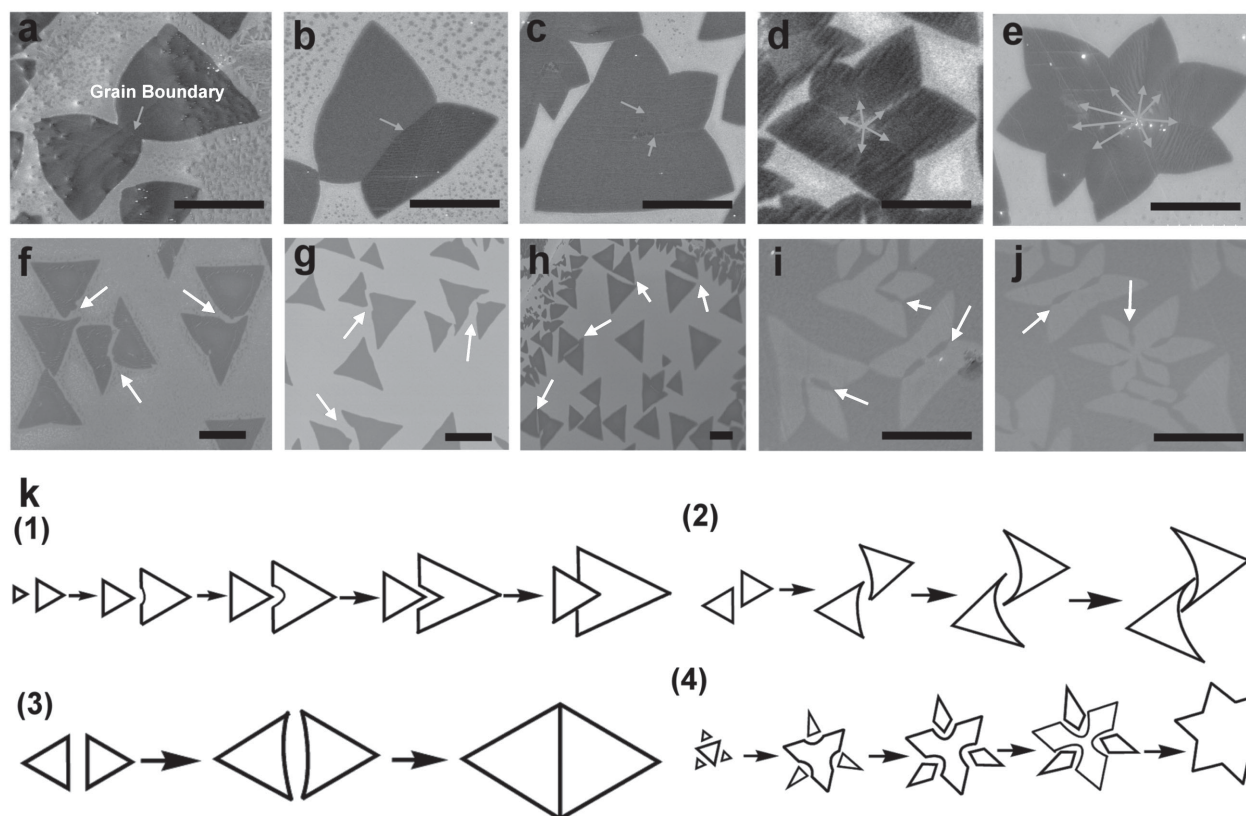


**Figure 5.** a–e) Typical SEM images of h-BN flakes with various complex structures. Note that grain boundary lines can be seen and labeled by arrows. f–h) SEM images showing several cases of close-distanced h-BN flakes on Cu surface. i, j) SEM images of lock and key structure formed before the complete merging of separated h-BN flakes. **Note that samples were air-oxidized, so the contrast of h-BN (the white part) with respect to Cu surface is reversed compared to that in (f–h).** k) The models for the dynamic merging process of h-BN flakes, where (1–3) represent cases for point-to-edge, partly and fully edge-to-edge merging. The model (4) describes a process for constructing perfect star-like structure using triangle building block. All the scale bars are 5  $\mu\text{m}$ .

process. Figure 5k shows three typical cases including point-to-edge (Figure 5k-1), partly (Figure 5k-2) and fully (Figure 5k-3) edge-to-edge merging modes. Note that when they eventually merge, grain boundaries are formed. Under a condition of air-oxidized h-BN/Cu surface, these grain boundaries can be clearly identified in SEM images as shown in Figure 5a–e. In contrast, AFM images of these merged h-BN flakes transferred onto 300 nm  $\text{SiO}_2/\text{Si}$  (Figure S12, Supporting Information) show no sign of continuous lines of grain boundaries. Finally, a complex structure could be constructed by repeating this approach, and an example of building perfect star-like structure is shown in Figure 5k-4. It is also important to recognize that the merging of different-shaped h-BN flakes shown in Figure 2e exhibits the similar features with that of ideal triangle-shaped h-BN, indicating the generality of our proposed model.

In summary, we have experimentally demonstrated the unrevealed, well-behaved CVD growth, and  $\text{Ar}/\text{H}_2$  etching behavior for monolayer h-BN flakes and continuous film. These results shed light on the general growth and etching kinetics in 2D material systems. Remarkably, the detailed processes for merging h-BN flakes into continuous structures or film were firstly revealed and explained. This study is important for both tailoring 2D material properties by growth or etching and understanding the kinetic processes in the related systems.

## Experimental Section

Cu foils were first annealed in  $\text{Ar}/\text{H}_2$  environment for 6 h, and then they were loaded into 1 in. diameter CVD fused quartz tube. Once the desired growth temperatures were obtained, solid ammonia borane precursor placed in a quartz boat was heated to different temperatures (50, 70, 90, and 110  $^\circ\text{C}$ ) by a heating belt for the decomposition of the source. After certain period of growth time (typically 60–70 min), the single-crystal h-BN flakes and monolayer film were synthesized. The h-BN flakes were produced on Cu surface using ammonia borane CVD method at various conditions (see the Supporting Information). The h-BN etching process was described in the text. The transferring process of h-BN materials was reported previously by Wang et al.<sup>[12]</sup> The samples were characterized by XPS spectroscopy, Raman spectroscopy (Renishaw in Via Plus, with laser excitation at 514 nm and spot size of 1–2  $\mu\text{m}$ ), Fourier transform infrared spectroscopy (FTIR, a Nicolet Magna IR 750), optical microscopy, scanning electron microscopy (SEM, Hitachi S-4800, 1 and 15 kV), atomic force microscopy (AFM, Veeco Nanoman VS in the tapping mode), and transmission electron microscopy (Tecnai G2 F20 U-TWIN, operated at 200 kV).

## Supporting Information

Supporting Information is available from the Wiley Online Library or from the author.

## Acknowledgements

L.W. and B.W. contributed equally to this work. This work was supported by the National Basic Research Program of China (2011CB932700, 2011CB932303, and 2013CB933500), the National Natural Science Foundation of China (61171054, 21273243, 60911130231, 51233006, and 61390500), and the Strategic Priority Research Program of the Chinese Academy of Sciences (XDB12030100).

Received: March 10, 2015

Revised: June 21, 2015

Published online: July 17, 2015

- [1] K. S. Novoselov, D. Jiang, F. Schedin, T. J. Booth, V. V. Khotkevich, S. V. Morozov, A. K. Geim, *Proc. Natl. Acad. Sci. USA* **2005**, *102*, 10451.
- [2] A. K. Geim, I. V. Grigorieva, *Nature* **2013**, *499*, 419.
- [3] B. Wu, D. C. Geng, Z. P. Xu, Y. L. Guo, L. P. Huang, Y. Z. Xue, J. Y. Chen, G. Yu, Y. Q. Liu, *NPG Asia Mater.* **2013**, *5*, e36.
- [4] R. M. Jacobberger, M. S. Arnold, *Chem. Mater.* **2013**, *25*, 871.
- [5] B. Wu, D. C. Geng, Y. L. Guo, L. P. Huang, Y. Z. Xue, J. Zheng, J. Y. Chen, G. Yu, Y. Q. Liu, L. Jiang, W. P. Hu, *Adv. Mater.* **2011**, *23*, 3522.
- [6] X. S. Li, W. W. Cai, J. An, S. Kim, J. Nah, D. X. Yang, R. Piner, A. Velamakanni, I. Jung, E. Tutuc, S. K. Banerjee, L. Colombo, R. S. Ruoff, *Science* **2009**, *324*, 1312.
- [7] A. Reina, X. T. Jia, J. Ho, D. Nezich, H. Son, V. Bulovic, M. S. Dresselhaus, J. Kong, *Nano Lett.* **2009**, *9*, 30.
- [8] Z. Yan, Z. W. Peng, J. M. Tour, *Accounts Chem. Res.* **2014**, *27*, 1327.
- [9] D. G. Geng, B. Wu, Y. L. Guo, B. R. Luo, Y. Z. Xue, J. Y. Chen, G. Yu, Y. Q. Liu, *J. Am. Chem. Soc.* **2013**, *135*, 6431.
- [10] D. C. Geng, B. Wu, Y. L. Guo, L. P. Huang, Y. Z. Xue, J. Y. Chen, G. Yu, L. Jiang, W. P. Hu, Y. Q. Liu, *Proc. Natl. Acad. Sci. USA* **2012**, *109*, 7992.
- [11] K. Watanabe, T. Taniguchi, H. Kanda, *Nat. Mater.* **2004**, *3*, 404.
- [12] L. F. Wang, B. Wu, J. S. Chen, H. T. Liu, P. A. Hu, Y. Q. Liu, *Adv. Mater.* **2014**, *24*, 1559.
- [13] K. K. Kim, A. Hsu, X. T. Jia, S. M. Kim, Y. M. Shi, M. Dresselhaus, T. Palacios, J. Kong, *ACS Nano* **2012**, *6*, 8583.
- [14] G. Kim, A-Rang. Jang, H. Y. Jeong, Z. Lee, D. J. Kang, H. S. Shin, *Nano Lett.* **2013**, *13*, 1834.
- [15] M. Wang, S. K. Jang, W. J. Jang, M. Kim, S. Y. Park, S. W. Kim, S. J. Kahng, J. Y. Choi, R. S. Ruoff, Y. J. Song, S. Lee, *Adv. Mater.* **2013**, *25*, 2746.
- [16] Y. M. Shi, C. Hamsen, X. T. Jia, K. K. Kim, A. Reina, M. Hofmann, A. L. Hsu, K. Zhang, H. N. Li, Z. Y. Juang, M. S. Dresselhaus, L. J. Li, J. Kong, *Nano Lett.* **2010**, *10*, 4134.
- [17] K. K. Kim, A. Hsu, X. T. Jia, S. M. Kim, Y. M. Shi, M. Hofmann, D. Nezich, F. Joaquin, M. Dresselhaus, T. Palacios, J. Kong, *Nano Lett.* **2012**, *12*, 161.
- [18] R. Y. Tay, X. L. Wang, S. H. Tsang, G. C. Loh, R. S. Singh, H. Li, G. Mallick, E. H. T. Teo, *J. Mater. Chem. C* **2014**, *2*, 1650.
- [19] W. Auwärter, H. U. Suter, H. Sachdev, T. Greber, *Chem. Mater.* **2004**, *16*, 343.
- [20] Y. Gao, W. C. Ren, T. Ma, Z. B. Liu, Y. Zhang, W. B. Liu, L. P. Ma, X. L. Ma, H. M. Cheng, *ACS Nano* **2013**, *7*, 5199.
- [21] A. Ismach, H. Chou, D. A. Ferrer, Y. P. Wu, S. McDonnell, H. C. Floresca, A. Covacevich, C. Pope, R. Piner, M. J. Kim, R. M. Wallace, L. Colombo, R. S. Ruoff, *ACS Nano* **2012**, *6*, 6378.
- [22] C. H. Zhang, L. Fu, S. L. Zhao, Y. Zhou, H. L. Peng, Z. F. Liu, *Adv. Mater.* **2014**, *11*, 1776.
- [23] R. Y. Tay, M. H. Griep, G. Mallick, S. H. Tsang, R. S. Singh, T. Tumlin, E. H. T. Teo, S. P. Karna, *Nano Lett.* **2014**, *14*, 893.
- [24] F. Baitalow, J. Baumann, G. Wolf, K. Jaenicke-Robler, G. Leitner, *Thermochem. Acta* **2002**, *391*, 159.
- [25] S. Frueh, R. Kellett, C. Mallery, T. Molter, W. S. Willis, C. King'odu, S. L. Suib, *Inorg. Chem.* **2011**, *50*, 783.
- [26] L. Ci, L. Song, C. Jin, D. Jariwala, D. Wu, Y. Li, A. Srivastava, Z. F. Wang, K. Storr, L. Balicas, F. Liu, P. M. Ajayan, *Nat. Mater.* **2010**, *9*, 430.
- [27] X. B. Wang, C. Y. Zhi, L. Li, H. B. Zeng, C. Li, M. Mitome, D. Golberg, Y. Bando, *Adv. Mater.* **2013**, *25*, 4072.
- [28] L. L. Jiang, B. Wu, H. T. Liu, Y. Huang, J. Y. Chen, D. C. Geng, H. J. Gao, Y. Q. Liu, *Adv. Mater.* **2013**, *25*, 7015.
- [29] Y. Satio, *Statistical Physics of Crystal Growth*, World Scientific, Singapore **1996**.
- [30] P. Sutter, J. Lahiri, P. Albrecht, E. Sutter, *ACS Nano* **2011**, *9*, 7303.
- [31] S. J. Harris, G. L. Doll, D. C. Chance, A. M. Weiner, *Appl. Phys. Lett.* **1995**, *67*, 2314.
- [32] C. Y. Zhi, Y. Bando, C. C. Tang, D. Golberg, R. G. Xie, T. Sekigushi, *Appl. Phys. Lett.* **2005**, *86*, 213110.
- [33] Y. Zhang, Y. F. Zhang, Q. Q. Ji, J. Ju, H. T. Yuan, J. P. Shi, T. Gao, D. L. Ma, M. X. Liu, Y. B. Chen, X. J. Song, H. Y. Hwang, Y. Cui, Z. F. Liu, *ACS Nano* **2013**, *7*, 8963.
- [34] A. M. van der Zande, P. Y. Huang, D. A. Chenet, T. C. Berkelbach, Y. M. You, G. H. Lee, T. F. Heinz, D. R. Reichman, D. A. Muller, J. C. Hone, *Nat. Mater.* **2013**, *12*, 554.
- [35] S. Najmaei, Z. Liu, W. Zhou, X. L. Zou, G. Shi, S. D. Lei, B. I. Yakobson, J. C. Idrobo, P. M. Ajayan, J. Lou, *Nat. Mater.* **2013**, *12*, 754.